Springer Geophysics

Shuanggen Jin
Nader Haghighipour
Wing-Huen Ip *Editors*

Planetary Exploration and Science: Recent Results and Advances

Springer

Springer Geophysics

More information about this series at http://www.springer.com/series/10173

Shuanggen Jin • Nader Haghighipour
Wing-Huen Ip
Editors

Planetary Exploration and Science: Recent Results and Advances

Springer

Editors
Shuanggen Jin
Shanghai Astronomical Observatory
Chinese Academy of Sciences
Shanghai, China

Bulent Ecevit University
Zonguldak, Turkey

Wing-Huen Ip
National Central University
Taoyuan, Taiwan

Nader Haghighipour
University of Hawaii-Manoa
NASA Astrobiology Institute
Honolulu, HI, USA

ISBN 978-3-662-45051-2 ISBN 978-3-662-45052-9 (eBook)
DOI 10.1007/978-3-662-45052-9
Springer Heidelberg New York Dordrecht London

Library of Congress Control Number: 2014957128

Printed on acid-free paper

Springer is part of Springer Science+Business Media (www.springer.com)

Preface

With the development of space techniques, more and more curious solar system bodies are being explored by humans. For example, several countries have launched orbiters and landers to the moon recently, focusing on unprecedented resources, origins and evolutions of the moon, including Japan's SELenological and ENgineering Explorer (SELENE), China's Chang'E-1/2/3 and India's Chandrayaan-1 and US's Lunar Reconnaissance Orbiter (LRO) and Gravity Recovery and Interior Laboratory (GRAIL). These missions provided direct observations on space environments, surface processes, rocks and minerals, water ice, interior structure and the origin of the moon. Furthermore, a number of upcoming lunar missions programmes have been planned, e.g., India's Chandrayaan-2, (2014), Russia's Lunar Glob 1 and 2 (2014/2015), China's Chang' E-4 (2017), and International Lunar Network (2018), which will enable us to answer more unknown questions on lunar exploration and sciences. In addition, with recent Mars Global Surveyor (MGS), Mars Express, Mars Odyssey, Mars Reconnaissance Orbiter (MRO), Venus Express, Phoenix, and so on, the atmosphere, surface processes and interior structure of the Mars, Venus and other planets were well explored and understood. However, the origin, formation and evolution on planets and exoplanets are still unclear, as well as seeking life beyond Earth.

This book will present the recent developments of planetary exploration techniques and the latest results on planetary science as well as future objectives of planetary exploration and science, e.g., lunar surface iron content and Mare Orientale basalts, Earth's gravity field, Martian radar exploration, crater recognition, ionosphere and astrobiology, exoplanetary atmospheres and planet formation in binaries. It will help readers to quickly familiarize themselves with the field of planetary exploration and science. In addition, it is also useful for planetary probe designers, engineers and other users' community, e.g., planetary geologists and geophysicists. This work was supported by the National Basic Research Program of China (973 Program) (Grant No. 2012CB720000) and Main Direction Project

of Chinese Academy of Sciences (Grant No. KJCX2-EW-T03). Meanwhile, we would like to gratefully thank Springer Publisher for their processes and cordial cooperation to publish this book.

Shanghai, China — Shuanggen Jin
Honolulu, HI, USA — Nader Haghighipour
Chung-Li, Taiwan — Wing-Huen Ip
May 2015

Contents

About the Editor

Shuanggen Jin is a Professor at the Shanghai Astronomical Observatory, CAS and Bulent Ecevit University, Turkey. He received the B.Sc. degree in Geodesy/Geomatics from Wuhan University in 1999 and the Ph.D. degree in GNSS/Geodesy from University of Chinese Academy of Sciences in 2003. His main research areas include satellite navigation, remote sensing, satellite gravimetry and space/planetary exploration as well as their applications. He has published over 200 papers in JGR, IEEE, EPSL, Icarus, GJI, JG, Proceedings etc., seven books/monographs and seven patents/software copyrights. He has been President of the International Association of Planetary Sciences (IAPS) (2013–2017), Chair of the IAG Sub-Commission 4.6 (2011–2015), Editor-in-Chief of *International Journal of Geosciences*, Associate Editor of *IEEE Transactions on Geoscience and Remote Sensing* (2014–), Associate Editor of *Journal of Navigation* (2014–), Associate Editor of *Advances in Space Research* (2013–), Editorial Board member of *Journal of Geodynamics* (2014–), *Planetary and Space Science* (2014–) and other seven international journals. He has received Special Prize of Korea Astronomy and Space Science Institute (2006), 100-Talent Program of Chinese Academy of Sciences (2010), Fellow of International Association of Geodesy (IAG) (2011), Pujiang Talent Program of Shanghai (2011), Fu Chengyi Award of Chinese Geophysical Society (2012), Second Prize of Hubei Natural Science Award (2012), Second Prize of National Geomatics Science and Technology Progress Award (2013/2014), Outstanding Young Scientist Award of Scientific Chinese (2013), Liu Guangding Geophysical Youth Science and Technology Award (2013), and Second Prize of Shanghai Science and Technology Progress Award (2014).

Chapter 1
Partial Least Squares Modeling of Lunar Surface FeO Content with Clementine Ultraviolet-Visible Images

Lingzhi Sun and Zongcheng Ling

Abstract To accurately predict the iron abundance of the Moon has long been the goal for lunar remote sensing studies. In this paper, we present a new iron model based on partial least squares regression (PLS) method and apply this model to map the global lunar iron distribution using Clementine ultraviolet-visible (UVVIS) dataset. Our iron model has taken into account of more calibration sites other than Apollo and Luna sample-return sites and stations (i.e., the six additional highland or immature sites) in combination with more spectral bands (5 bands and 2 band ratios), in order to derive reliable FeO content and improve the robustness of the PLS model. By comparing the PLS-derived iron map with Lucey's band-ratio FeO map and Lawrence's Lunar Prospector (LP) FeO map, the differences are mostly within 1 wt% in FeO content. Moreover, PLS-derived FeO is more consistent with LP's result which was derived by direct measurement of Fe gamma-ray line (7.6 MeV) rather than the Lucey's experiential algorithm applying only two bands (750, 950 nm) of Clementine UVVIS dataset. With a global mode of 5.1 wt%, PLS-derived iron map is also validated by FeO abundances of lunar feldspathic meteorites and in support of the lunar magma ocean hypothesis.

Keywords Lunar iron content • Partial least squares regression (PLS) • Spectroscopy • Clementine UVVIS

1.1 Introduction

As one of the major rock-forming elements, iron is closely related to lunar mafic mineral assemblages and rock types; thus the accurate estimation of iron abundance would provide important information of lunar geochemistry, petrogenesis, as well

L. Sun • Z. Ling (✉)
School of Space Science and Physics, Shandong Provincial Key Laboratory of Optical Astronomy and Solar-Terrestrial Environment, Institute of Space Sciences, Shandong University, Weihai 264209, China
e-mail: zcling@sdu.edu.cn

S. Jin et al. (eds.), *Planetary Exploration and Science: Recent Results and Advances*, Springer Geophysics, DOI 10.1007/978-3-662-45052-9_1

as the crustal evolution. Iron is often expressed as FeO in astrochemistry. The absorption properties in the ultraviolet-visible (UVVIS) and near-infrared (NIR) spectral regions of iron-bearing minerals (e.g., pyroxene, olivine, and ilmenite) are dominated by Fe^{2+} or Ti^{4+}/Ti^{3+} (Lucey et al. 1998). The absorption features from lunar sample or remotely sensed spectra would mix up influences from the exposures of lunar soils to the space environment, i.e., the Moon has been suffering from bombardments by micrometeorites, solar wind ions, cosmic rays, and solar flare particles (Fischer and Pieters 1994, 1996). Sustained bombardments will cause the lunar surface material change in petrography and chemistry. These changes include reduction of mean grain size, the production of nanophase iron ($npFe^0$) and complex glass-welded aggregates of lithic and mineral fragments (agglutinates), and so on (Fischer and Pieters 1994, 1996; Mckay et al. 1974). This so-called process "space weathering" will bring about the maturation of lunar regolith, i.e., the mature regolith usually has suffered from a longer time of space weathering compared to immature regolith. Space weathering will cause an overall reduction in the reflectance, and reduce the absorption band strengths, creating and steepening a red-sloped continuum (Fischer and Pieters 1994, 1996).

Many authors have obtained the empirical relationships between spectral properties and iron abundance of lunar soils with intent to get a more accurate lunar iron model (Lucey et al. 1995, 2000; Blewett et al. 1997; Gillis et al. 2004; Wilcox et al. 2005). Lucey et al. (1995) firstly provided a method for the derivation of iron from Clementine multispectral images, utilizing the laboratory spectra and iron abundance of lunar soils. A Fe parameter was defined based on compositional and maturity-related trends on a plot of 950 nm/750 nm versus 750 nm reflectance, which was found to have a strong linear relationship with iron abundance (Fig. 1.1) (Lucey et al. 1995). It can be seen from Fig. 1.1 that iron content has an orthogonal effect, where low iron abundance has high reflectance and high ratio whereas high iron abundance has low reflectance and low ratio. This trend has a hypothetical

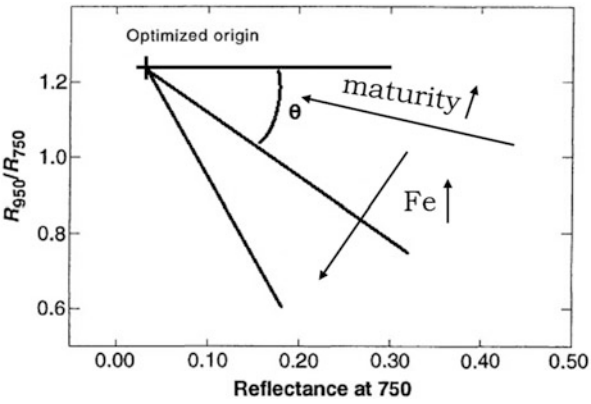

Fig. 1.1 A schematic diagram of NIR/VIS ratio versus VIS for lunar samples. Samples with high iron abundance toward *lower left* on the plot. Samples with same iron abundance but different maturities locate along a line radial to a dark red mature end-member at the *upper left*. The Fe parameter (θ) could decouple iron content from maturity

end-member ("Optimized origin" in Fig. 1.1), which is dark and "red." However, Blewett et al. (1997) pointed it out that the directional-hemispherical laboratory spectra that Lucey used in his algorithm may induce error when applying to the bidirectional spacecraft measurements. He improved Lucey's method by collecting image of lunar landing sites and applying them to iron mapping algorithms. Lucey et al. (1998) examined and quantified important aspects, e.g., maturity, grain size and mineralogy, and topographic shading, in his new iron modeling. He then obtained an improved iron abundance model by using their final processing of Clementine UVVIS datasets (Lucey et al. 2000). Later on, Gillis et al. (2004) noted that TiO_2 abundance has an effect on the relationship between Fe content and Fe parameter, and they optimized this method by adding TiO_2-sensitive regression parameters into the regression of iron content. Wilcox et al. (2005) developed a new algorithm to determine the iron content in lunar mare regions based on the findings that the maturity trends in lunar mare area are more parallel than radial. They collected more than 9,000 craters from mare regions and make a 950/750 nm vs. 750 nm reflectance plot with these data and found the radial trends were disobeyed. While iron abundance was still orthogonal to maturity trends, the maturity trends were parallel to each other, suggesting new trends of iron distribution in lunar mare. Their new iron model has absolute uncertainty similar to Lucey 2000's model (1.5 wt%), while it allows better compensation for the maturity-induced iron uncertainties (<0.5 wt%).

Except for NIR/VIS ratio methods mentioned above, many other approaches like utilizing infrared continuum slope of the spectrum in order to suppress the effect of topography (Le Mouelic et al. 2002) and iron absorption band depth (Fischer and Pieters 1994) have been proposed in the iron modeling. These methods are limited by the data calibration and quality of Clementine NIR dataset. Statistical relationships between spectral and chemical abundance of lunar soils have also been evaluated by Pieters et al. 2002 for their applications of remotely compositional analysis. She firstly applied principle component analysis (PCA) regression method with lunar mare soil spectra produced by Lunar Soil Characterization Consortium (LSCC) to define and evaluate the correlations between chemical abundance and spectral parameters (Pieters et al. 2002). Then she also derived three statistical relations between spectral and mineral parameters using LSCC data and applied them to Clementine UVVIS data (Pieters et al. 2006).

Although many iron models have been put forward as discussed above, a quantitatively accurate iron model is still in need, especially for the exploration of the potentials of multispectral imaging data like Clementine UVVIS and other lunar hyperspectral datasets (e.g., data from Moon Mineralogy Mapper (M^3), Interference Imaging Spectrometer (IIM), etc.). In this paper, we choose to build iron abundance models with partial least squares (PLS) regression method. PLS is known as the second generation of regression method, which performs well in multivariable regression especially when multiple correlations exist among variables. Li (2006) made a comparison between PLS and PCA in deriving chemical and mineral abundances using data from LSCC. He found PLS models use less components

and perform better than PCA in the estimation of lunar chemical and mineral abundances. However, Li didn't apply his result to lunar remotely sensed images. Our PLS-derived iron model is developed with intent to explore the potential of the UVVIS imaging dataset. During the modeling, we find it is easy to reach a good regression relationship (high correlation efficient (R^2) value) between spectra parameters and iron contents, while maturity suppressing is more difficult to attain. We have tested many different variables in PLS modeling to find the most applicable one for Clementine UVVIS images and compare our results with previous studies to evaluate the robustness of the PLS model.

1.2 Data

The lunar remote sensing images used in this study are from Clementine UVVIS Digital Image Model (DIM) published by US Geological Survey (USGS) Astrogeology Team at Flagstaff, Arizona (NASA PDS Geosciences Node). The DIM has five bands with a nominal ground resolution at 100 m/pixel, and the center wavelengths (spectra resolutions) of the five filters are A, 415 nm (40 nm); B, 750 nm (10 nm); C, 900 nm (20 nm); D, 950 nm (30 nm); and E, 1,000 nm (30 nm) (Eliason et al. 1999). This dataset is archived in the NASA Planetary Data System, and each image has undergone radiometric and geometric correction, spectral registration, and photometric normalization by Integrated Software for Imagers and Spectrometers (ISIS) processing system.

The PLS modeling data points include those extracted from Apollo and Luna sampling stations (from Wilcox et al. (2005), Table 2) and supplementary data from farside highlands and optically fresh (immature) areas (shown in Table 1.1). From our experiments, the statistical prediction of chemical abundance rely significantly on the input variables, i.e., an obvious deviation of iron abundance would appear when the modeling didn't include data points from farside highland and immature areas. Note that the iron abundances of supplementary data in Table 1.1 were calculated with Lucey's (2000) parameters.

Table 1.1 Iron abundance and reflectance values of supplementary data from Clementine UVVIS

	Clementine spectra					
Sites	415 nm	750 nm	900 nm	950 nm	1,000 nm	FeO (wt%)
Farside-1	0.1196	0.2022	0.2178	0.2250	0.2302	2.3
Farside-2	0.1195	0.2032	0.2183	0.2271	0.2336	1.7
Farside-3	0.1330	0.2271	0.2372	0.2447	0.2546	3.8
Fresh-1	0.0794	0.1265	0.1140	0.1108	0.1111	17.2
Fresh-2	0.0767	0.1229	0.11155	0.1088	0.1103	17.4
Fresh-3	0.0811	0.1353	0.1202	0.1174	0.1203	16.8

1.3 Partial Least Squares Regression Method and Data Processing

PLS is a new kind of multivariate statistics regression method, which was developed by Herman Wold in 1966 (Li 2006). Comparing to other regression methods (like PCA regression), PLS has many advantages, especially in resolving mutual influence problems among variables. PLS has already been utilized for analyzing material compositions from laboratory and remote sensing spectra datasets. Li (2006, 2008) resampled LSCC bidirectional reflectance data into the airborne visible/infrared imaging spectrometer (AVIRIS) spectral resolution and derived several composition derivation models such as iron and TiO_2 with PLS regression method (Li 2006, 2008, 2011). Li's model was based on laboratory data and was not applied to remotely sensed data, making it difficult to evaluate the ability of the model in maturity suppressing.

As an advanced statistical method, the principle of PLS analyzing can be expressed as: PLS = PCA + CCA + MLR (CCA, classical component analysis; MLR, multiple linear regression). The key to PLS modeling is to determine the number of latent variables (LVs), which are also called the components. Covariance between each corresponding component of independent variable and dependent variable should be kept maximum; this can be considered as a combination of LVs searching conditions of PCA and CCA.

Assuming the independent variance is an $n \times m$ matrix X, and dependent variance is an $n \times p$ matrix Y, we first standardize matrixes X and Y before modeling in order to reach a more stable result. Following PLS rules while regressing X and Y, finally, we can get the relations listed below (Eqs. 1.1 and 1.2). Both X and Y are decomposed into two parts: a matrix product term and a residual term. The matrix product term consists of a score matrix and a loading matrix, score matrixes are T for X and U for Y, and they are both $n \times a$ matrixes; loading matrixes are P for X and Q for Y, and they are both $m \times a$ matrixes. E and F are residual matrixes. The goal of regression is to find the correlative relation between X and Y (Eq. 1.3) while keeping residual matrixes E and F minimum:

$$X = TP^T + E = \sum_a t_a p_a^T \tag{1.1}$$

$$Y = UQ^T + F = \sum_a u_a q_a^T \tag{1.2}$$

$$Y = XB + F \tag{1.3}$$

In order to find better relations between spectral data and iron content, we transfer reflectance spectra into effective absorbance spectra first. With zero transmittance given, absorbance can be roughly expressed as log reflectance based on Beer's Law (Eq. 1.4), where R denotes reflectance and α is absorbance. The derived absorbance

α is assumed to have a linear relationship with the abundance of composition (Li 2006; Yen et al. 1998; Whiting et al. 2004; Milliken and Mustard 2005):

$$-\ln R = -\ln(1-\alpha) \tag{1.4}$$

1.4 PLS Modeling

1.4.1 Iron Modeling

In our PLS model, modeling data points including 47 lunar sampling sites from Wilcox et al. (2005) and 6 added data from lunar farside highlands and fresh areas, so there are 53 modeling sites in total, and X is a 53×5 matrix, and Y is a 53×1 matrix. After transforming reflectance into absorbance, we standardized both X and Y in order to get a more stable model. While modeling, the most important thing is to derive reasonable iron content as well as suppress the space weathering effect at the same time. All of the five bands are included in the dependent variables to keep the maximum potential, and they are expressed by $A_1 - A_5$, respectively. Band ratios are helpful especially when extracting chemical abundances, and they are also indications of maturity degree. Our model takes account of the typical NIR/VIS ratio (950 nm/750 nm), which is used in Lucey's algorithm. Pieters et al. (2002) have tested the correlations between composition and spectral ratios, and experiments showed that the highest correlation for iron is 1,000/400 nm. Hence, we also bring it into our model, expressed by 1,000/415 nm. Finally, all the variables chosen to build model are listed in Eq. 1.5, $c_0 - c_7$ are regression coefficients, and $A_1 - A_5$ represent five absorption bands of Clementine data:

$$\text{Iron} = c_0 + \sum_{i=1}^{5} A_i c_i + \left(\frac{A_4}{A_2}\right) c_6 + \left(\frac{A_5}{A_1}\right) c_7 \tag{1.5}$$

After inputting all the data into PLS toolbox, leave-one-out cross-validation is executed during modeling. The cross-validation means modeling with one variable left out until all the variables have been left out once; thus we would derive a regression model in each cross-validation and compute the root mean square error of cross-validation (RMSECV) for every leave-one-out model by Eq. 1.6; k is the number of variable that is left out. Usually, the one with minimum RMSECV will be chosen as the best LV number. After the number of components is determined, the total root mean square (RMSE) can be calculated by Eq. 1.7.

Figure 1.2 is the plot of RMSE and RMSECV values, the minimum RMSECV is 1.51 wt%, and the corresponding LV number is 1. Measured abundances of iron and those derived from the PLS model are plotted in Fig. 1.3. Correlation coefficient

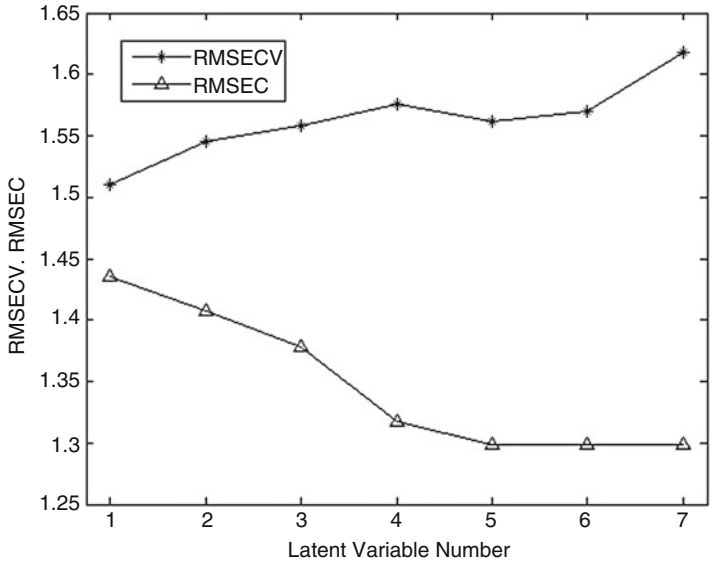

Fig. 1.2 RMSE and RMSECV distribution plot. The minimum RMSECV is 1.51, indicating the optimal number of LVs is 1

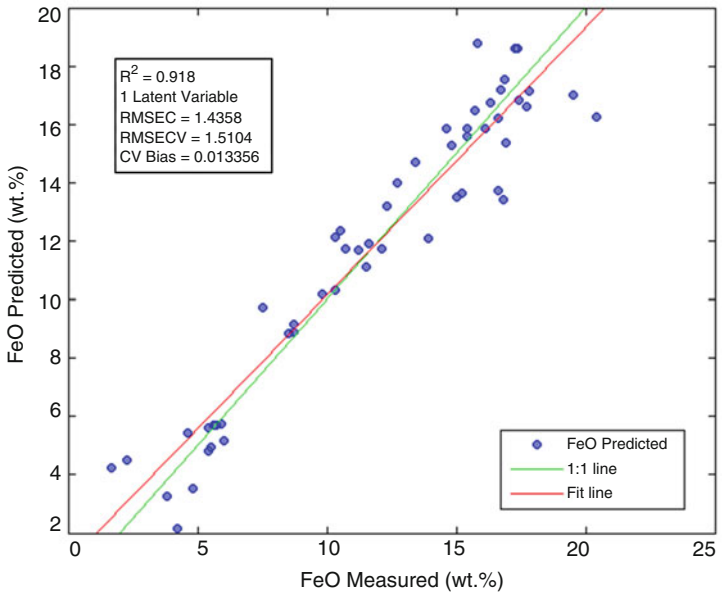

Fig. 1.3 Regression result of PLS modeling. The correlation coefficient is 0.918, and RMSE is 1.44, and RMSECV is 1.51

(R^2) of this model is 0.918, and RMSE is 1.44 wt%, indicating a good regression of iron abundance has been achieved:

$$\mathrm{RMSECV}_k = \sqrt{\frac{\sum_{i=1}^{8} (\widehat{y}_i - y_i)_k^2}{8}} \tag{1.6}$$

$$\mathrm{RMSE} = \sqrt{\frac{\sum_{i=1}^{8} (\widehat{y}_i - y_i)^2}{8}} \tag{1.7}$$

1.4.2 Results and Analysis

We apply the PLS model mentioned in Sect. 1.4.1 to a small area near the southern rim of Mare Crisium (Fig. 1.4a) for preliminary check and validation. This region is chosen for two reasons. First, its location is near the boundary of mare and highland, so bimodal distribution of FeO is expected to exist; moreover, there are many small spectrally fresh craters (low maturity degree) in the mare area, which could be used as an indicator for the maturity-suppressing ability of our model (Ling et al. 2011).

PLS-derived iron map is shown in Fig. 1.4c in comparison with the result of Lucey's work (Fig. 1.4b). Considering the maturity-suppressing ability can be indicated by the small fresh craters in the mare region, the difference between our model and Lucey's is subtle, i.e., most of small fresh craters (bright spots in the 750 nm reflectance image (Fig. 1.4a)) are invisible in the PLS-derived FeO map in Fig. 1.4b, c. The distribution of FeO in the mare area is relatively homogenous, which indicates that the maturity-suppressing ability of our model is comparable to Lucey's algorithm.

It can be seen from Figs. 1.4 and 1.5 that FeO abundance is high in mare regions and low in highland regions. Generally, FeO abundance of mare regions is higher than 10 wt%, which is due to the large concentration of iron-bearing silicates in mare basalts such as pyroxene, olivine, ilmenite, etc. Highland region is deficient in iron, as its rock type is dominated by anorthosite (Lucey et al. 1995, 1998). From the histogram of iron abundance (Fig. 1.5), we can distinguish a bimodal distribution of FeO in this region; the peak on the left represents FeO concentration in highland region and right peak represents that in mare region. Comparing the PLS model to Lucey et al.'s (2000) algorithm, it can be recognized that the two models have similar peak positions for the mare region (right peak), and the peak FeO abundances are about ~16.5 wt%; while the FeO abundances for the highland (left peak) have a little difference, our result is around 9 wt%, about 1 wt% higher than Lucey's. This discrepancy may result from various causes such as model input parameters (e.g., different bands or sampling sites). Further discussions will be given in Sect. 1.4.3.

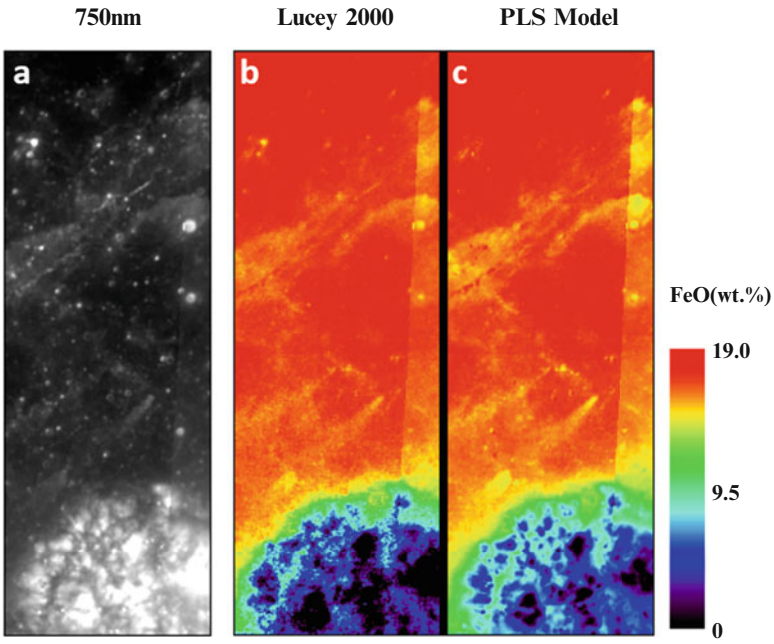

Fig. 1.4 (**a**) 750 nm reflectance of a small area from southern Mare Crisium, (**b**) iron map derived from Lucey's algorithm, and (**c**) iron map derived from PLS model. It can be seen that most of the bright fresh craters are invisible in our iron map

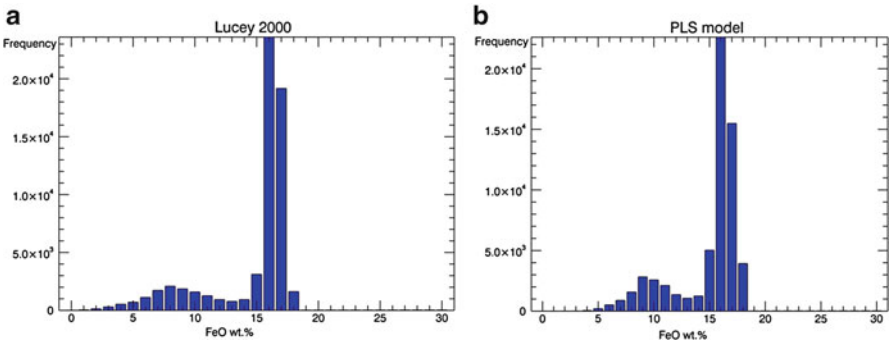

Fig. 1.5 Statistical result of Fig. 1.4 (**a**) Lucey's result, corresponding to Fig. 1.4b; (**b**) our result, corresponding to Fig. 1.4c. Both of them have obvious bimodal structure, the left peak represents iron concentration in highland area, and the right peak represents iron concentration in mare area. Iron peak in highland area is 9 wt% in our model and 8 wt% in Lucey's, while iron peak in mare area is about 16.5 wt%, which is the same with Lucey's

1.4.3 PLS Modeling of Highland Areas

As discussed above, although the two iron maps behave similarly in iron abundance and maturity suppressing, they still exhibit discrepancy in FeO modeling of highland regions. The iron abundance of our model for highland region is a little higher than Lucey's, which is shown both in iron map (Fig. 1.4b, c) and the statistical results of iron map (Fig. 1.5). As is known to all, statistical methods strongly depend on the sampling data points, i.e., when the sampling data points lack of a specific range of FeO abundance, the result may tend to behave deviate from that range. During the modeling, although six supplementary data are added for lunar sampling stations, the highland data sources are only composed of Apollo 16 sampling stations and 3 added lunar farside sites. The limited proportion of highland spectra to the total modeling data may lead to the overestimation of iron abundance in highland areas during the PLS modeling. To testify this hypothesis, we derive another iron model using only Apollo 16 and Apollo 17 sampling sites, in order to increase the proportion of highland sampling sites. Data processing pipeline follows the first PLS model (Eq. 1.5).

Applying this highland model to test area, we derive a new iron map. Iron abundance derived by highland model (Fig. 1.6c) is obviously less than that

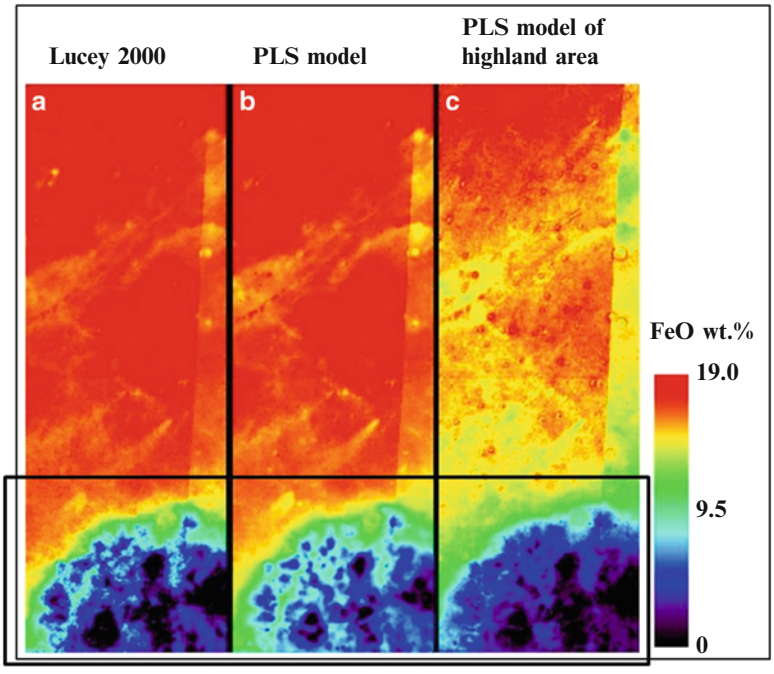

Fig. 1.6 Iron map comparison, highland regions are indicated by a black frame. (**a**) Lucey's result; (**b**) the first PLS model result; (**c**) highland modeling result. The iron abundance of **c** in the highland regions is obviously less than **b** and **a**

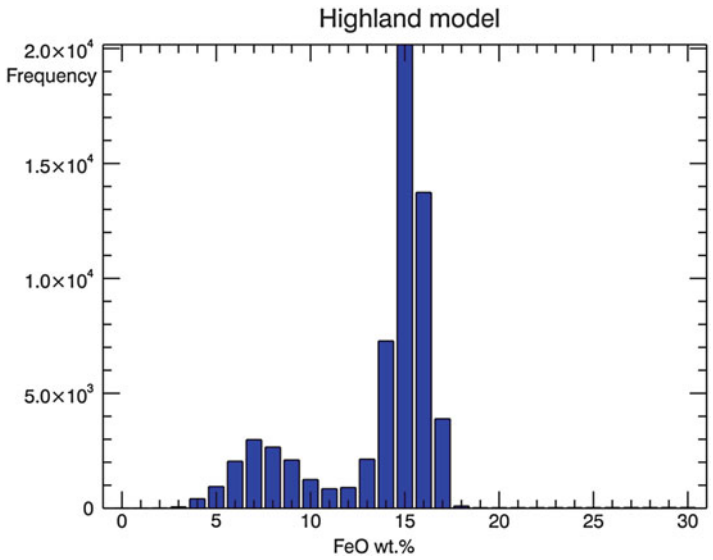

Fig. 1.7 Statistical result of iron abundance of the model build with highland spectra. The FeO abundance peak of highland region is 7 wt%, which is lower than the first model (Fig. 1.6b, 9 wt%) as well as Lucey's result (Fig. 1.6a, 8 wt%)

modeling with all the data presented in Table 1.1 (Fig. 1.6b). From the statistical results, we can find that the iron concentration peak of highland regions reduces to 7 wt% (Fig. 1.7), as compared to the former 9 wt% (Fig. 1.5b). Given the proportion of highland data increases and PLS regression procedures remain the same, we can conclude that the PLS model relies on the input modeling data, i.e., the spectral types and iron abundances range of the modeling data could affect PLS model behavior significantly. Although it looks like one can improve the PLS modeling behavior by adding supplementary data to the original lunar sampling sites, the number of added data should be in caution. As stated above, elemental abundance of added data is usually calculated by empirical methods, which may induce uncertainty or even correct conclusions. We have done tens of experiments with the number of data points varying from dozens to hundreds; the PLS model presented in Sect. 1.4.1 is the best one when all the available Apollo and Luna ground truth data are considered. As supplementary data for highlands and fresh areas, the added data only accounts for a very small proportion in the modeling data compared to lunar sampling stations. For future work, we will focus on trying to find more effective variables or anticipating more typical sampling sites in the future missions.

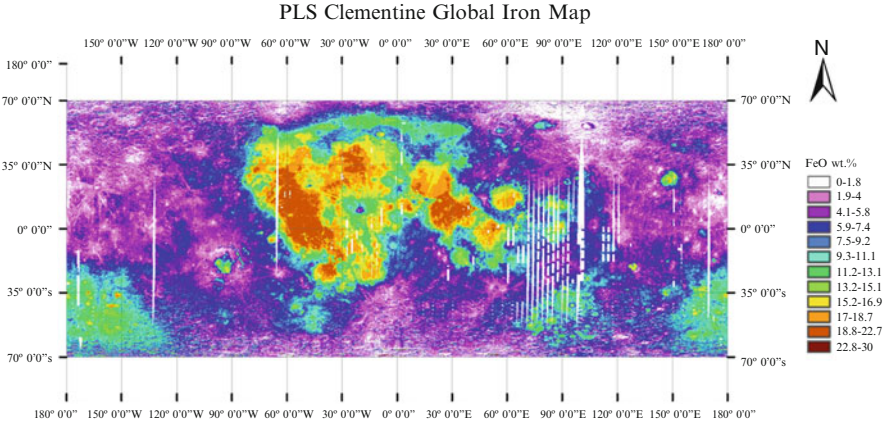

Fig. 1.8 Global iron map of PLS model. Data greater than 30.0 wt% or less than 0.0 wt% are set to NAN (not a value) in this map

1.5 Global Iron Mapping and Analysis

1.5.1 Global Iron Mapping

Applying the PLS model from Sect. 1.4.1 to Clementine DIM global mosaic, we can obtain a lunar global iron map (Fig. 1.8). As shown in Fig. 1.8, FeO is obviously rich in the large basins that spread in lunar nearside such as Mare Imbrium, Oceanus Procellarum, Mare Serenitatis, Mare Tranquillitatis, etc., all of which are known to have been flooded by large amounts of iron-rich basalt lava flow. The histogram of global iron distribution is shown in Fig. 1.9c. Global mean FeO abundance is 7.6 wt% by PLS model. The bimodal structure represents decoupled iron distribution in mare and highland region. The global mode of FeO is 5.1 wt%, corresponding to the left peak in Fig. 1.9c, and FeO abundance peak in mare is 16.9 wt%, corresponding to the right peak.

1.5.2 Comparison with Former Works

To understand more about the global FeO map derived from PLS model, we compare our work with Lucey's band-ratio result and Lunar Prospector (LP) (Figs. 1.10 and 1.11; Table 1.2). On a global view, the global mean of FeO abundance of PLS model is 7.6 wt%, and the value is 7.8 wt% for both Lucey's and LP's results. Peak values of FeO in the highland (global mode) are 5.1 wt% for PLS model and 6.4 wt% for LP, while Lucey's algorithm derives a relatively lower value less than 5 wt%. Peak distribution of FeO in the mare for the three model is

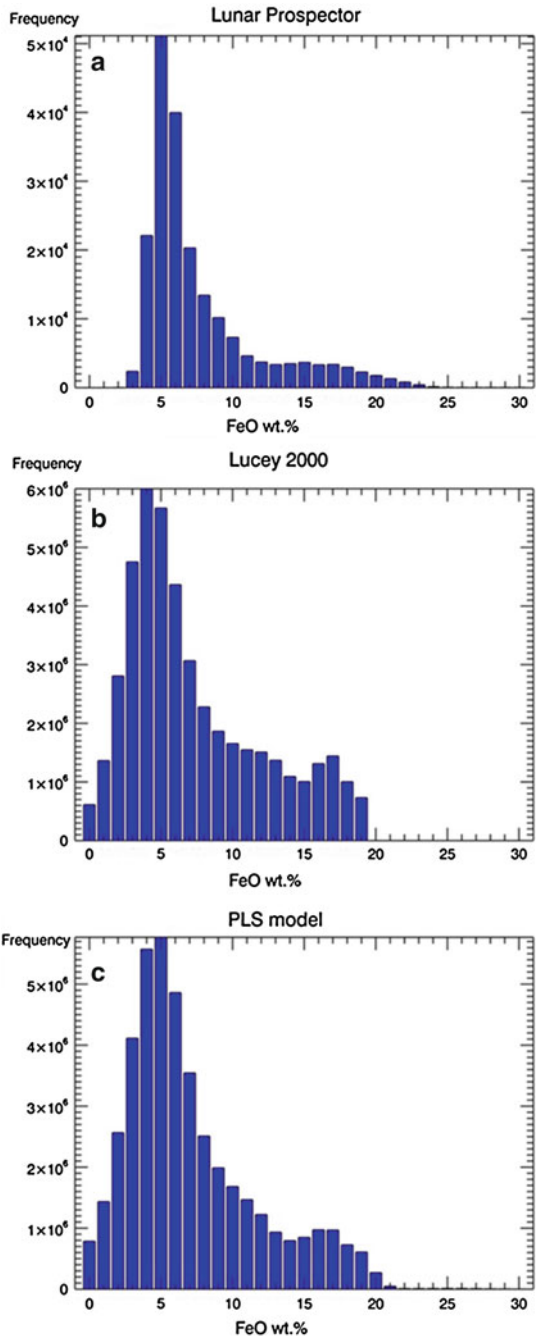

Fig. 1.9 Comparison of statistical results. (**a**) Global histogram of FeO from LP, (**b**) Lucey 2000, (**c**) PLS modeling

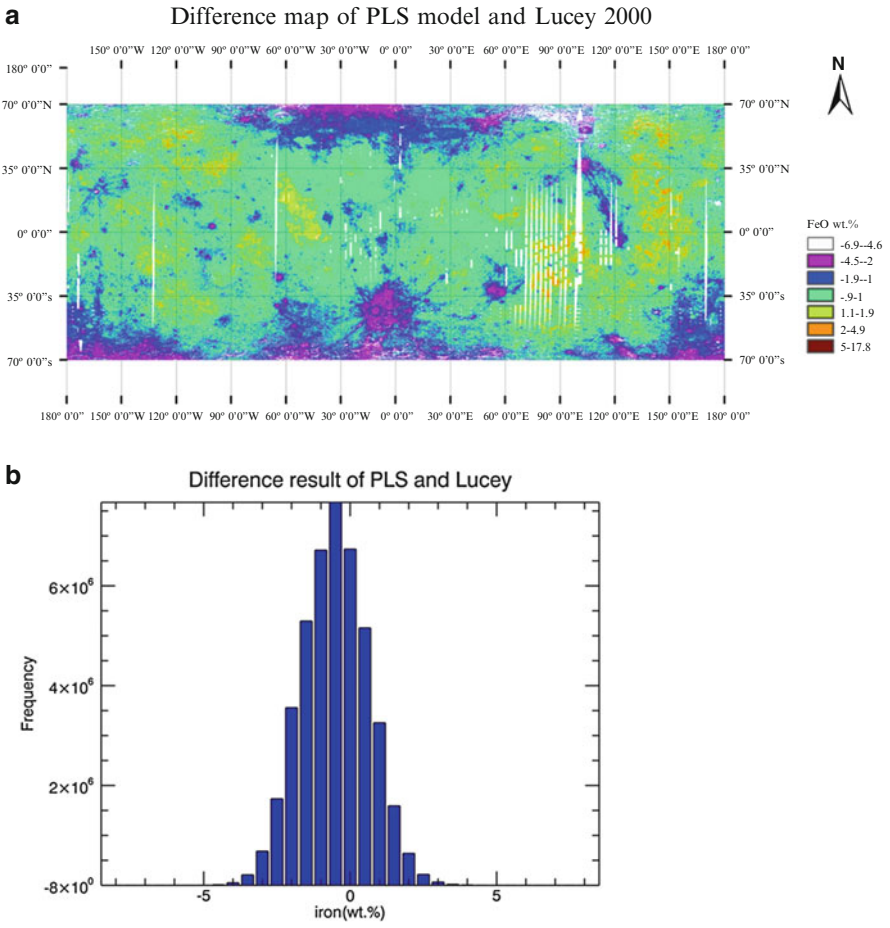

Fig. 1.10 (**a**) Difference map between iron map derived from PLS model and Lucey's algorithm (PLS minus Lucey's). (**b**) The difference of the two maps shows a Gaussian distribution with an average of 0.27 wt%, and RMS is 1.13 wt%

around 17 wt%. Comparing from the statistical results (Fig. 1.9), FeO abundance derived by PLS model in lunar highland areas is a little higher than Lucey's but is similar to LP's. Detail comparisons between PLS model, Lucey's algorithm, and LP result will be discussed in the following.

In order to show the global difference between PLS model and Lucey's method, we apply Lucey's algorithm to Clementine DIM and make a difference map (PLS FeO minus Lucey's FeO), as shown in Fig. 1.10a. Most of the difference distributes within −0.9 to 1.0 wt% which is shown in green color in the difference map. PLS model gets an even higher iron abundance than Lucey's result in lunar farside, which is consistent with the statistical result comparison (Fig. 1.9b, c). Another

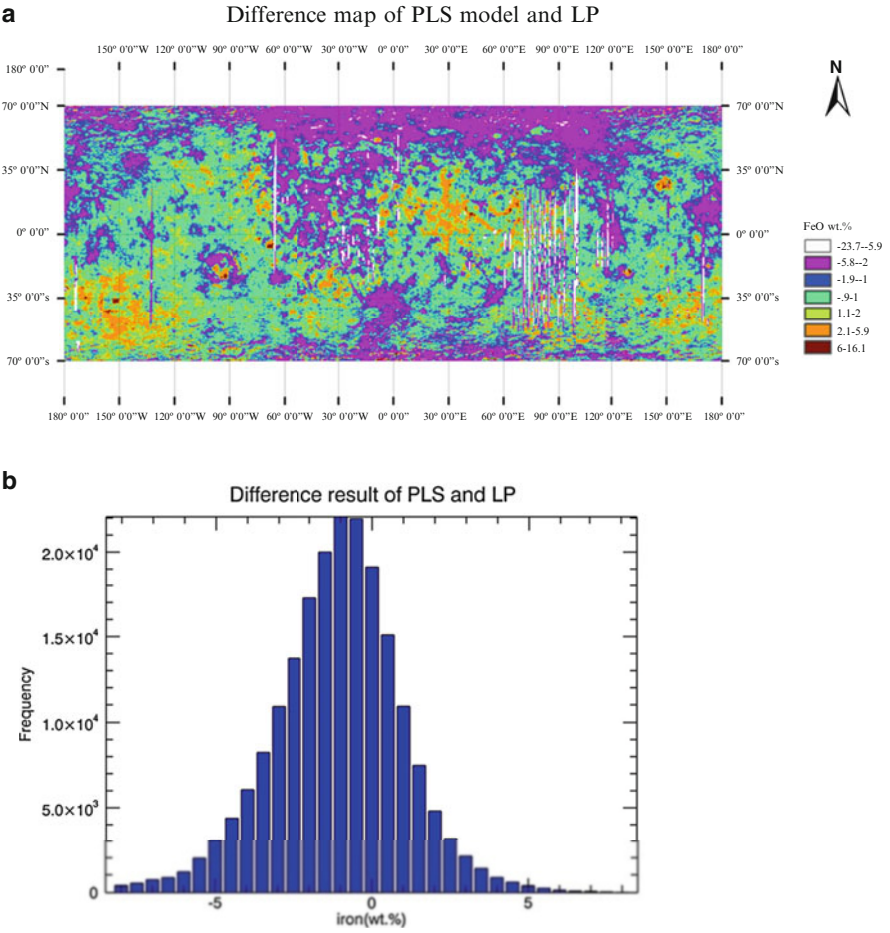

Fig. 1.11 (**a**) Difference map between iron map derived from PLS model and Lunar Prospector gamma-ray spectrometer (PLS minus Lucey's). (**b**) Statistical result of a, suggest an average of 0.9 wt% and RMS is 2.3 wt%

Table 1.2 Comparison of FeO abundance between different algorithms

FeO model	Global mean (wt%)	Global mode (wt%)	Peak value in mare (wt%)
Lucey 2000	7.8	4.7	17.1
Lunar Prospector	7.8	6.4	17
PLS model	7.6	5.1	16.9

discovery from the difference map is that iron in fresh craters derived by PLS is often lower than Lucey's result, represented by Tycho crater (located in south-southwest of the map, about 43.3°S, 11.2°W). This may be caused by different degrees of maturity suppressing between the two methods. Statistical result (Fig. 1.10b) shows a nearly Gaussian distribution of the difference, with an average value around −0.27 wt%, and root mean square error (RMS) is 1.13 wt%, indicating a relatively small difference of the global iron abundance between the two maps.

Lawrence et al. (2002) derived a global iron map from the gamma-ray counting rate of the lunar surface detected by Lunar Prospector (LP). The Fe derived by gamma-ray spectrometer is a direct measurement of Fe gamma-ray line (7.6 MeV). Moreover, gamma-ray spectrometer usually detects signal from over 10 cm below lunar regolith, so the result would be less affected by space weathering effect, making the FeO abundance more reliable than that derived by experienced algorithms. The global mode of LP is 6.4 wt%, compared to 5.1 wt% derived from PLS model. Comparing to Lucey's result, iron abundance derived by PLS modeling is more consistent with that detected by LP as far as highland regions are considered. In other words, the higher iron value that is derived from PLS model for the lunar highland regions when compared to Lucey's algorithm may suggest a more reliable result. As for iron distribution of Tycho crater, Lawrence et al. (2002) also found a large discrepancy, i.e., Lucey's results show moderate FeO abundances at 7–9 wt%, while the LP data show very low FeO abundances at 3–4 wt%. FeO content from PLS modeling is about 3.8 wt% which supports the LP result (Fig. 1.12a, b).

Considering the different spatial resolutions of the FeO maps from the spectral and gamma-ray datasets, in order to compare in detail with iron map derived by LP, we resample the Clementine iron map derived by PLS to the same spatial resolution as LP iron map (15 km/pixel) and make a global difference map (regions exceed 70°S–70°N are not included) (Fig. 1.11a). The difference distribution on the global map isn't very homogenous, but when we take a look at the global iron distribution, we find the global difference is concentrated within −0.9 to 1.0 which is colored by green, and iron abundance detected by LP in mare areas and high-latitude regions is higher than PLS model. The difference in high latitudes tends to be greater; this effect may be the influence of topographic shading or illumination conditions.

Furthermore, our iron content of PLS model for the South Pole-Aitken (SPA) basin is higher than LP's but lower than Lucey's (Fig. 1.12c). As the largest impact crater on the Moon, the SPA impact event didn't penetrate the materials from lunar mantle, which are expected to be more mafic and iron rich. The specific noritic mineralogy may account for this low FeO concentration (Lucey 2004). From the statistical result of the difference map, the global average of iron difference is within 1 wt% and the RMS is 2.3 wt%, suggesting a good consistency of PLS model and LP iron map.

In a word, we find the iron map from PLS model agrees with those from the Lucey's and LP's, though subtle difference appears for the global maps. This suggests our PLS model is a robust algorithm for the extraction of lunar iron content. Furthermore, the application of PLS method on the global lunar mosaic seems to be more consistent with LP results than those of Lucey 2000. Note that our PLS model

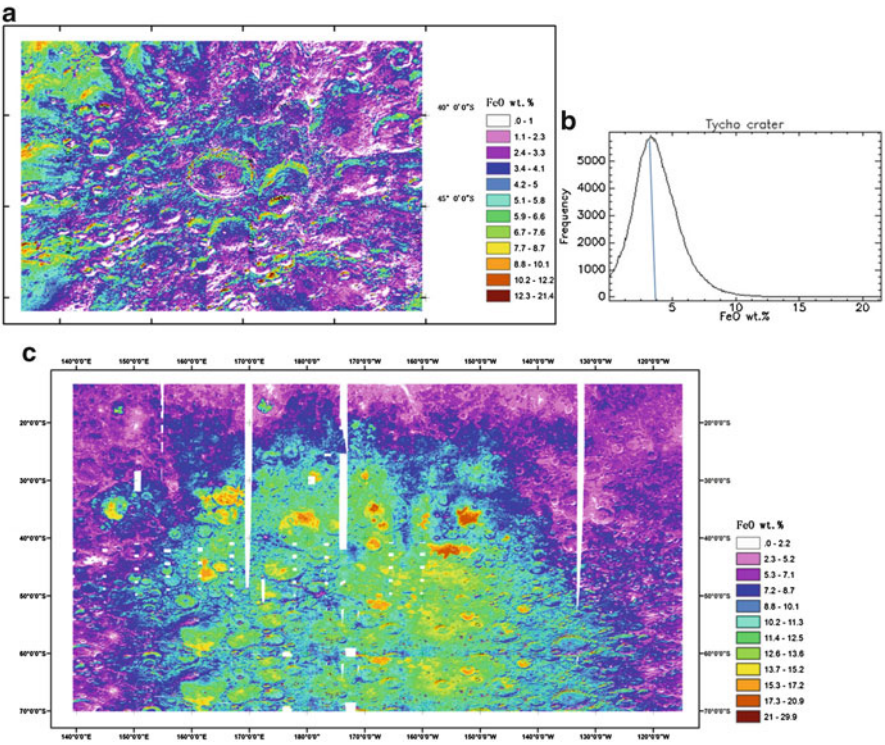

Fig. 1.12 (**a**) PLS-derived iron map of Tycho crater; (**b**) statistical result of iron distribution in Tycho crater; (**c**) PLS-derived iron map of SPA region

explored the potential for all the five available Clementine UVVIS bands and some more spectral parameter than Lucey et al. (2000), who used only Clementine's two bands (950 and 750 nm) to derive iron content. We believe our PLS model is a good test and validation for the lunar elemental mapping with available lunar spectral data and those from future lunar missions.

1.6 Indication of Lunar Magma Ocean Hypothesis

After lunar sample returned to earth, a lot of laboratory experimental analyses have been done to extract information of the lunar mineralogy and petrogenesis, which are very helpful in understanding lunar origin and evolution progress in a global or local scale. Samples from lunar highland regions contain higher plagioclase abundance and hence are rich in Al and poor in Fe compared to those from mare regions (Lucey et al. 1995). These rocks are interpreted as forming from a global circling magma ocean, and plagioclase floated in it (Wood et al. 1970; Warren

and Haskin 1991). The magma ocean hypothesis was developed following the first sample return from the Moon. The crystallization of the magma ocean would result in FeO poor anorthosite rocks concentrating in the crust.

As was mentioned by Lucey et al., the key test of the magma ocean hypothesis is the abundance of anorthosite (Lucey et al. 1995). Usually, anorthosite assembles in lunar highlands, so iron abundances in these regions could represent the global anorthosite concentration. In remote detection, the global mode of FeO concentration represents iron abundance of lunar highland regions. The global mode of iron abundance derived by Lucey et al. in 1995 is about 3 wt% (in Fe, and 3.96 wt% in FeO), and he improved the algorithm in year 1998, and the new global mode of FeO is 4.8 wt% (Lucey et al. 1998). These results are consistent with our result (5.1 wt%). As far as lunar meteorites study are concerned, Korotev et al. studied eight best characterized feldspathic lunar meteorites and showed the average concentration of FeO is 4.4 ± 0.5 wt%, and the FeO range is 3–6 wt% (Korotev et al. 1996; 2003; Korotev 2005). The global mode of PLS-derived FeO map is 5.1 wt%, which also agrees well with meteorite studies and remote sensing results (Lucey et al. 1995, 1998, 2000; Lawrence et al. 2002) and thus could also support the magma ocean hypothesis of lunar crust.

1.7 Conclusions

We derived a new iron model with PLS method, which has been verified to be able to derive robust iron abundances for the Moon. We apply this model to Clementine DIM and obtain global distribution of iron. Our results show that peak distribution of iron abundance in highlands and mare regions are 5.1 wt% and 16.9 wt%, respectively. Comparing our iron map to Lucey's algorithm as well as that detected by Lunar Prospector gamma-ray spectrometer, we find the three results agree well in mare regions, while PLS model and LP iron maps show higher iron content in highlands. Local comparisons (e.g., Tycho crater and SPA basin) also suggest our PLS model is reliable and more consistent with the LP results. Besides, the PLS model-derived iron abundance peak of lunar farside is 5.1 wt%, which agrees well with the lunar meteorites that are assumed from lunar highland. Our global FeO distributions are also consistent with the lunar magma ocean hypothesis as has been presented by previous work (Lucey et al. 1995, 1998; Wood et al. 1970; Warren and Haskin 1991).

Although our PLS algorithms have already shown its potential for extraction of lunar iron abundance, it should be kept in mind that there are limitations, i.e., the exact physical significance of PLS is not as evident as experience algorithms, and PLS regression highly depends on the type of the modeling data inputs. More lunar samples and precise geographic location of them would definitely contribute to the improvement of PLS modeling for iron. Interference Imaging Spectrometer (IIM) onboard Chang'E-1 has achieved the abundance of some key elements of the Moon (Ling et al. 2011; Wu et al. 2012; Jin et al. 2013). As is known, China's new

lunar lander and rover mission, "Chang'E-3" lander and "Yutu" rover, respectively, have launched in December 2013, and the rover will be released to detect mineral distribution of the lunar surface, especially in Sinus Iridum (Liu et al. 2013), which has never been set foot on by any lander or rover before. Spectral data from VIS-NIR Imaging Spectrometer (VNIS) onboard Yutu rover may provide good opportunities and more constraints for lunar compositional studies and as PLS modeling of lunar iron abundance as well.

Acknowledgements This work was supported by the National Natural Science Foundation of China (11003012, U1231103), the Natural Science Foundation of Shandong Province (ZR2011AQ001), Independent Innovation Foundation of Shandong University (2013ZRQP004), and Graduate Innovation Foundation of Shandong University at WeiHai, GIFSDUWH (yjs13026).

References

Blewett DT, Lucey PG, Hawke BR (1997) Clementine images of the lunar sample-return stations: refinement of FeO and TiO_2 mapping techniques. J Geophys Res 102(E7):16319–16325

Eliason E, Isbell C, Lee E et al (1999) The Clementine UVVIS global lunar mosaic. Cited 20 May 2013. http://www.lpi.usra.edu/lunar/tools/clementine/instructions/UVVIS_DIM_Info.html

Fischer EM, Pieters CM (1994) Remote determination of exposure degree and iron concentration of lunar soils using VIS-NIR spectroscopic methods. Icarus 111(2):475–488

Fischer EM, Pieters CM (1996) Composition and exposure age of the Apollo 16 Cayley and Descartes regions from Clementine data: normalizing the optical effects of space weathering. J Geophys Res 101(E1):2225–2234

Gillis JJ, Jolliff BL, Korotev RL (2004) Lunar surface geochemistry: global concentrations of Th, K, and FeO as derived from lunar prospector and Clementine data. Geochim Cosmochim Acta 68(18):3791–3805

Jin SG, Arivazhagan S, Araki H (2013) New results and questions of lunar exploration from SELENE, Chang'E-1, Chandrayaan-1 and LRO/LCROSS. Adv Space Res 52(2):285–305

Korotev RL (2005) Lunar geochemistry as told by lunar meteorites. Chemie der Erde 65:297–346

Korotev RL, Jolliff BL, Rockow KM (1996) Lunar meteorite Queen Alexandra Rang 93069 and the iron concentration of the lunar highlands surface. Meteorit Planet Sci 31:909–924

Korotev RL, Jolliff BL, Jolliff RA (2003) Feldspathic lunar meteorites and their implications for compositional remote sensing of the lunar surface and the composition of the lunar crust. Geochim Cosmochim Acta 67(24):4895–4923

Lawrence DJ, Feldman WC, Elphic RC (2002) Iron abundances on the lunar surface as measured by the Lunar Prospector gamma-ray and neutron spectrometers. J Geophys Res 107(E12):5130

Le Mouelic S, Lucey PG, Langevin Y (2002) Calculating iron contents of lunar highland materials surrounding Tycho crater from integrated Clementine UV-visible and near-infrared data. J Geophys Res 107:E10,5074

Li L (2006) Partial least squares modeling to quantify lunar soil composition with hyperspectral reflectance measurements. J Geophys Res 111:E04102

Li L (2008) Quantifying lunar soil composition with partial least squares modeling of reflectance. Adv Space Res 42:267–274

Li L (2011) Quantifying TiO_2 abundance of lunar soils: partial least squares and stepwise multiple regression analysis for determining causal effect. J Earth Sci 22(5):549–565

Ling Z, Zhang J, Liu J et al (2011) Preliminary results of FeO mapping using imaging interferometer data from Chang'E-1. Chin Sci Bull 56(4–5):376–379

Liu B, Liu J, Zhang G et al (2013) Reflectance conversion methods for the VIS/NIR imaging spectrometer aboard the Chang'E-3 lunar rover: based on ground validation experiment data. Res Astron Astrophys 13(7):862–874

Lucey PG (2004) Mineral maps of the moon. Geophys Res Lett 31:L08701

Lucey PG, Taylor GJ, Malaret E (1995) Abundance and distribution of iron on the moon. Science 268(5214):1150–1153

Lucey PG, Blewett DT, Hawke BR (1998) Mapping the FeO and TiO_2 content of the lunar surface with multispectral imagery. J Geophys Res 103(E3):3679–3699

Lucey PG, Blewett DT, Jolliff BL (2000) Lunar iron and titanium abundance algorithms based on final processing of Clementine ultraviolet–visible images. J Geophys Res 105(E8):20297–20305

Mckay DS, Fruland RM, Heiken GH (1974) Grain size and the evolution of lunar soils. In: Proceedings of the lunar science conference 3rd, Pergamon Press, New York, pp 983–995

Milliken RE, Mustard JF (2005) Quantifying absolute water content of minerals using near-infrared reflectance spectroscopy. J Geophys Res 110:E12001

NASA PDS Geosciences Node ftp://pds-geosciences.wustl.edu/geocopy/imaging/clem1-l-u-5-dim-uvvis-v1.0/cl_4001/catalog/

Pieters CM, Stankevich DG, Shkuratov YG et al (2002) Statistical analysis of the links among lunar mare soil mineralogy, chemistry, and reflectance spectra. Icarus 155:285–298

Pieters CM, Shkuratov Y, Kaydash V et al (2006) Lunar soil characterization consortium analysis: pyroxene and maturity estimates derived from Clementine image data. Icarus 184:83–101

Warren PH, Haskin L (1991) Lunar chemistry. In: Heiken GH et al (eds) Lunar sourcebook. Cambridge University Press, Cambridge, pp 357–474

Whiting ML, Li L, Ustin SL (2004) Predicting water content using Gaussian model on soil spectra. Remote Sens Environ 89:535–552

Wilcox BB, Lucey PG, Gillis JJ (2005) Mapping iron in the lunar mare: an improved approach. J Geophys Res 110:E1101

Wood JA, Dickey JS, Jr, Marvin UB et al (1970) Lunar anorthosites and a geophysical model of the moon. In: Proceedings of the Apollo 11 lunar science conference, Pergamon Press, New York, pp 965–988

Wu Y, Xue B, Zhao B et al (2012) Global estimates of lunar iron and titanium contents from the Chang'E-1 IIM data. J Geophys Res 117:E02001

Yen AS, Murray BC, Rossman GR (1998) Water content of the Martian soil: laboratory simulations of reflectance spectra. J Geophys Res 103:11125–11133